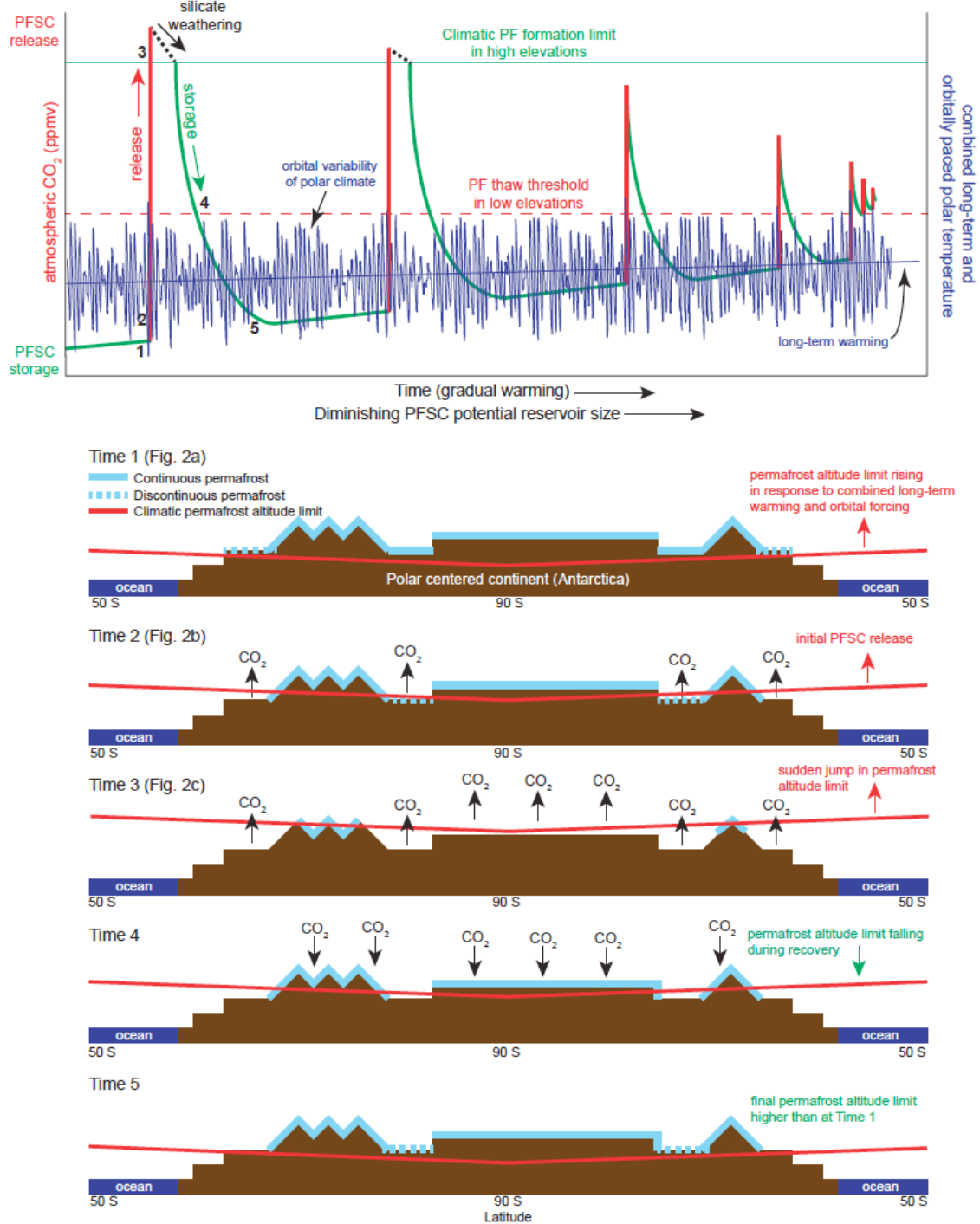# SUPPLEMENTARY INFORMATION

Correction notice

Past extreme warming events linked to massive carbon release from thawing permafrost

Robert M. DeConto, Simone Galeotti, Mark Pagani, David Tracy, Kevin Schaefer, Tingjun Zhang, David Pollard & David J. Beerling

In the version of the Supplementary Information originally posted online, Supplementary Table 1 contained an error. Peat carbon density (ρ) used in the ensemble of permafrost soil carbon calculations was listed as 140 kg m^{-3}. This is bulk peat density, not peat carbon density. The bulk density should have been multiplied by 0.5 kg C kg^{-1}, resulting in an average permafrost-peat carbon density of 70 kg m^{-3}. The correct value for peatland ρ in equation 3 doubles the estimated average thickness of permafrost peat deposits from 2.9 to 5.8 m. However, doubling the peat depth does not change the calculated carbon inventories discussed in the main text or in Table 2. The conclusions of the Letter remain unchanged. We thank S. Frolking for noting the ~50% underestimate of peat thickness, resulting from the use of bulk rather than carbon density. Supplementary Table 1 has been corrected in the new version of the Supplementary Information; see Supplementary Information Table of Contents for details.

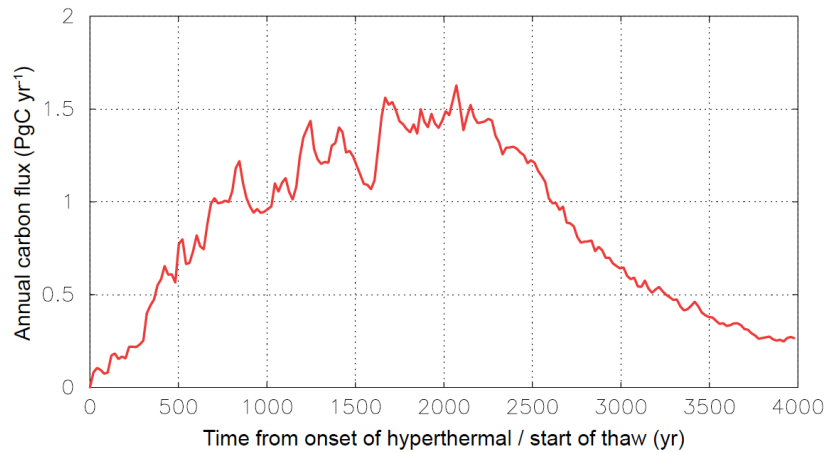## 1. Schematic diagram of the permafrost-hyperthermal mechanism

Supplementary Figure 1 | Schematic diagram illustrating the concepts presented in the paper. The top panel shows an idealized set of hyperthermal events (red and green), triggered when the combination of long-term warming and orbital forcing (blue lines)

drives polar temperatures beyond the permafrost stability threshold in higher elevations (red dashed line). Time is shown from oldest (left) to youngest (right). The first (largest) event represents ETM1 (PETM), although the sequence of hyperthermals is purely illustrative. For clarity, the duration and timing of the events are not to scale and the orbital time series of polar climatic forcing (blue) is synthetic, drawn to broadly mimic the timing of the hyperthermal events relative to the composite polar orbital forcing shown in Figure 1. This sequence is similar to the recently proposed pacing of marine hydrate release events[47], although the terrestrial mechanism proposed here is different. The numbers (1-5) correspond to the schematic cross-sections of Antarctica shown below.

Five schematic cross sections (bottom panels) represent the conditions on Antarctica through a typical hyperthermal sequence. Corresponding cross sections of the northern high latitudes (with polar ocean bounded by continents) are not shown, but the same coeval sequence applies. At time 1 (corresponding to conditions in Fig. 2a), the permafrost stability threshold (red dashed line) is first exceeded. As noted in the text, extreme high-eccentricity and high-obliquity orbits thaw permafrost in both hemispheres simultaneously, regardless of the seasonal timing of perihelion (precession). The available PFSC reservoir at time 1 is the largest, having accumulated for $>10^6$ years during the cooler climates of the late Palaeocene. The initial PFSC release at time 2 (Fig. 2b) causes additional GHG warming, leading to the release of almost the entire PFSC reservoir within 10^4 years (Time 3; Fig. 2c). Once the PFSC reservoir is exhausted, polar latitudes are too warm for permafrost to reform or for PFSC stocks to recharge until some initial cooling occurs. Initial drawdown of CO_2 must be driven by other mechanisms, such as silicate weathering (black dashed line), enhanced in response to extreme global warmth and elevated precipitation rates. Once enough initial cooling allows permafrost to begin reforming in higher elevations (below the horizontal green line), PFSC stocks begin to recharge quickly in a positive feedback of CO_2 drawdown, cooling and expanding PFSC storage in lower elevations, all during a period of attenuated orbital forcing. This sequence may explain carbon isotopic records of ETM1 (PETM) [9], indicating a ~100-kyr delay in the recovery of the carbon cycle after the main carbon input, followed by rapid-paced recovery over the next ~50 kyr[9]. At time 5, the PFSC reservoir reaches its maximum potential, but remains smaller than at time 1, because the background climate state is warmer. The gradual warming trend is ongoing until the Early Eocene Climatic Optimum (Fig. 1), implying successively smaller PFSC reservoirs (and smaller release events) until the polar regions become too warm (beginning in the north polar regions) to support permafrost, even in high elevations.

2. Rate of carbon release from thawing permafrost

Supplementary Figure 2 | Estimated annual fluxes of carbon from thawing permafrost for the first hyperthermal event (PETM/ETM1). Carbon release at the onset of the PETM is calculated over a time period of 4000 years, assuming the time history of annual fluxes would be similar to a transient simulation of large-scale permafrost thaw and potential permafrost carbon release based on the Intergovernmental Panel on Climate Change (IPCC) A1B scenario[27]. Annual fluxes are scaled to match the release of 3434 PgC in the orbitally triggered warming sequence depicted in Fig 2. The annual fluxes increase to a peak at ~2100 years, representing the maximum thaw rate, and subsequently decline as the rate of thaw decreases.
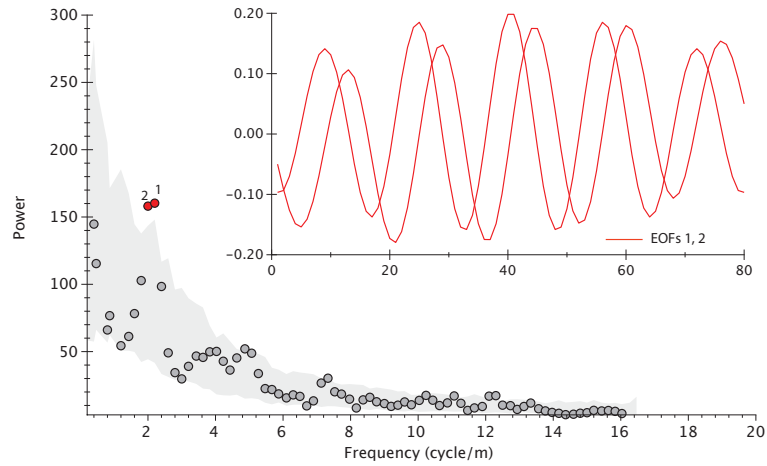
3. Composite Mean Summer Insolation Model

Assuming CO_2 release in high-latitude continental areas control the observed variability at Contessa Road and other sedimentary records, we estimate the effect of orbital forcing with a simple composite mean summer insolation model. The model assumes a linear relationship between changes in insolation and temperature, which is a conservative approach considering the enhanced climate sensitivity of high latitudes and the exponential relationship between soil temperature and background soil CH_4 emissions[48].

Because of different latitudinal distributions of polar continental areas between hemispheres, we use mean-summer insolation records at 75°S and 65°N from La04[18] for the time interval between 51.8-56.5 Ma, which includes ETM1, ETM2 and ETM3 and other minor hyperthermal-like events. To account for the larger extent of northern hemispheric land areas within orbitally sensitive high latitudes, we multiply the 65°N insolation curve by a factor of 2. Since Earth's orbital precession is antiphased between hemispheres, the resulting curve is dominated by obliquity (Fig 1e). A precessional signal is preserved because of the larger effect of the northern hemispheric curve, which accounts for geographic filtering. While variance at the 23-kyr precession period is observed in lower Eocene records[7,17,19], the orbital signal shows a weaker precessional component and becomes dominated by the 41 kyr obliquity period in time intervals corresponding with hyperthermals. These observations are well-matched by our GCM simulations (Fig. 1; Table 1), showing total global permafrost area is sensitive to obliquity forcing, once a threshold of background warming is reached. In the model, total permafrost area is most sensitive to a combination of high obliquity and high eccentricity (increased seasonality), with perihelion occurring in either January or July. The sensitivity of modeled permafrost to either intense summer insolation or longer summers (increased total integrated insolation) also has the effect of attenuating the precession signal, because total permafrost is reduced in both hemispheres simultaneously, regardless of the phase of precession. In this case, the smallest permafrost inventories at a given set of GHG levels occur during a combination of high obliquity and high eccentricity orbits, corresponding with the onset of hyperthermals shown in Figure 1.
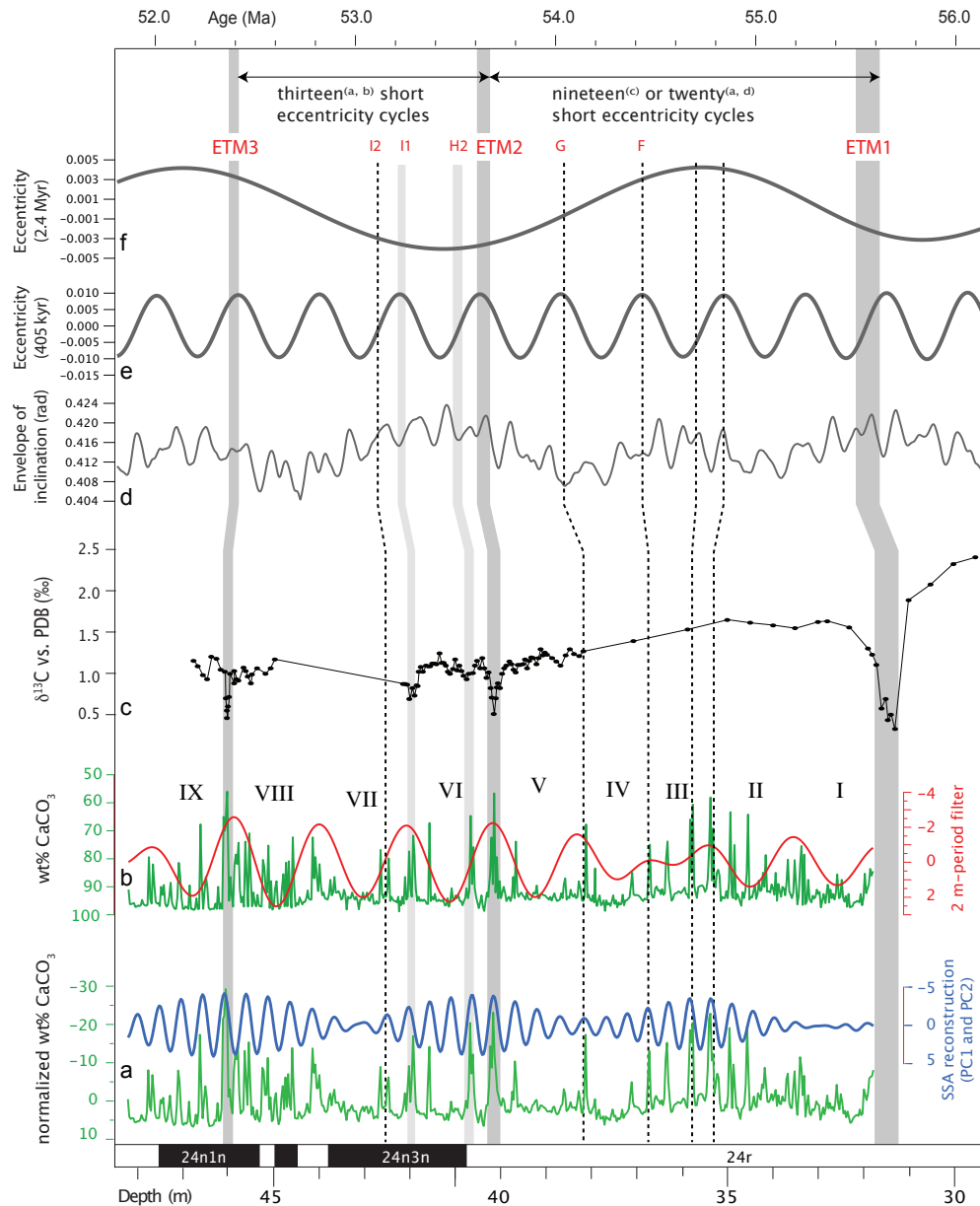
4. Singular Spectrum Analysis of the Wt% CaCO$_3$ Record

Singular spectrum analysis (SSA) is used to recognize harmonic components in the Wt% CaCO$_3$ record in the depth domain, which we validate using a Monte Carlo method[49] with a confidence limit of 97.5%. SSA is particularly well suited for the analysis of complex system showing non-linear oscillations on multiple time scales, like the climate system[50]. SSA is used here with an embedding dimension of 80. A longer embedding dimension would offer the advantage of detecting longer-term components and higher spectral resolution. However, an embedding dimension of 80 is a good choice for our series (550 points with 3 cm sampling rate) and an expected oscillatory period of ~50 cm for short eccentricity[7]. This approach provides a statistically robust means of detecting harmonic components in the range of orbital frequencies and their modulation before tuning (i.e. in the depth domain). Furthermore, cycle counting of the statistically significant components that are recognized to reflect orbital forcing offers an additional tool for comparison with previously published floating chronologies for the interval under investigation[17,19,51]. In the SSA, harmonic components typically occur as distinct oscillatory pairs of eigenvectors characterized by the same dominant frequency, similar eigenvalues, and a Pi/2 phase lag of their Empirical Orthogonal Functions (EOFs). Harmonic components have been identified in EOFs 1 and 2, both of which are above the 97.5% confidence level (Fig. S1), based on a Monte Carlo test against red-noise[49]. The sum of the two largest EOFs (EOF1 and EOF2) accounts for ~14% of the signal variance and the reconstructed component (Fig. S2) and shows a close correspondence to the original Wt% CaCO$_3$ signal. The SSA-reconstructed component also shows a distinct peak of spectral power with a period of ca. 0.48 metres, which is the period expected for the short eccentricity cycle based on a 4.7 m/Myr average sedimentation rate of the lower Eocene Contessa Road section as derived from independent (magneto- and bio-stratigraphic) dating[7]. The amplitude of short eccentricty cycles in the CaCO$_3$ record is modulated by a long-term forcing showing three maxima, all corresponding to hyperthermal events in the depth domain. Once the section is tuned in the time domain (based on cycle counting and an absolute age of 55.7 Ma for the base of ETM1)[7,19], these three modulation maxima (major hyperthermal events) coincide with the (sole) three maxima occurring in the composite mean summer insolation curve within the studied interval (see panel E in Figure 1 of the main text). A fourth maximum in the composite mean summer insolation is centered out of the surveyed interval at ~ 55.7 Ma at the onset of PETM, reinforcing the evidence for a 100% match between intervals of warmer summers at high latitudes and ETMs. Some uncertainty remains in terms of the absolute age of the ETMs and the astronomical solution (providing an absolute age of maxima in the composite mean summer insolation), however, the combined effect of the long-term components of eccentricity (400 kyr) and obliquity (1.2 Myr) produces a succession of high latitude insolation maxima that is 100% matched by the long-term cyclical architecture of lower Eocene sedimentary and geochemical records.
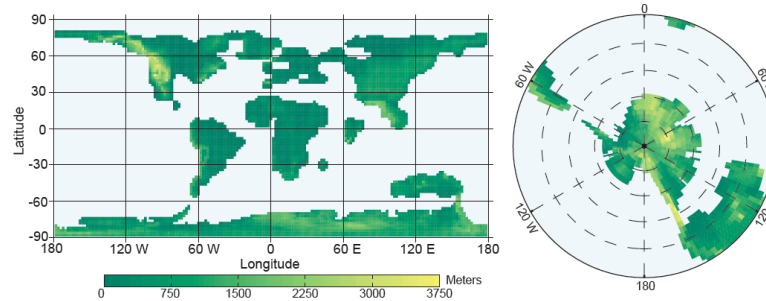
Supplementary Figure 3 | SSA Analysis. SSA Eigenspectrum and statistically significant (>97.5%) EOFs (inset) according to a red noise Monte Carlo Test of the $CaCO_3$ record.

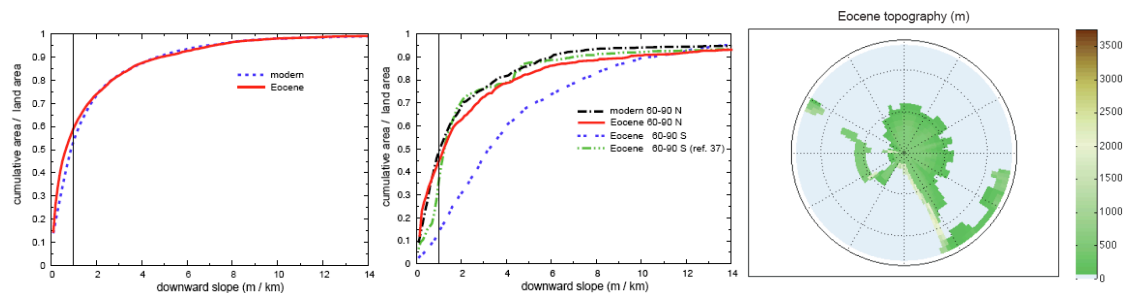## 5.   Orbital phasing of Early Eocene Hyperthermals

Supplementary Figure 4 | Orbital Phasing. The lower Eocene CaCO$_3$, δ^{13}C and magnetostratigraphic records from the Contessa Road section (lower panels). Extraction of the long eccentricity component (405 kyr; red line) from the CaCO3 record (green line) allows a fine-scale calibration to the long-term (405 kyr and 2.4 Myr) eccentricity components and the Hilbert transform of the obliquity from the La04[18] astronomical solution (top three panels). SSA reconstruction of the harmonic components (110 kyr; blue line) allows counting of individual eccentricity cycles. Maximum modulation occurs across intervals of concomitant high eccentricity and high obliquity, corresponding to the inferred position of CIE events in published cyclochronologies of the same interval[19,51-55]. The number of short eccentricity cycles counted in different sedimentary settings by a[55], b[7]; c[17], and d[51] are shown at top.
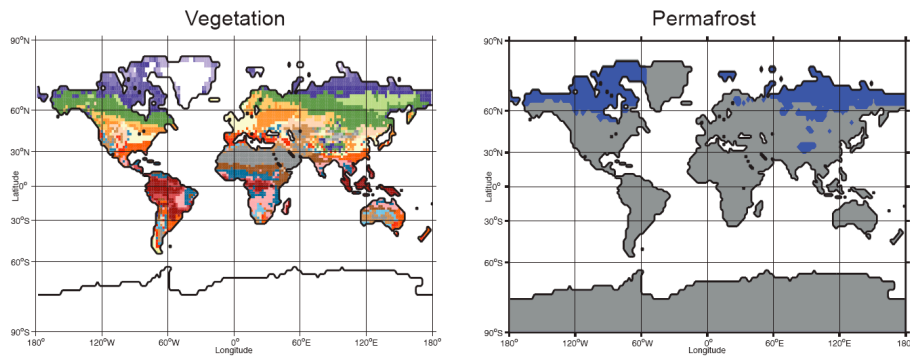
6. Model Boundary Conditions

Supplementary Figure 5 | Early Eocene global paleogeography. Palaeocene-Eocene climate-vegetation-permafrost simulations use a prior paleogeographic reconstruction of the Eocene[37,56], with Antarctic shorelines and elevations replaced with a new, larger reconstruction of West Antarctica in latest Eocene time[21]. The global 2º×2º cylindrical equidistant reconstruction used by the GCM surface model grid is shown at left, with a south polar view shown at right. In East Antarctica, where detailed geological data are lacking, the topography[21] is based on modern sub-glacial elevations, isostatically compensated to reflect ice-free conditions.

Supplementary Figure 6 | Palaeocene-Eocene hypsometry. The cumulative (fractional) land area below a given surface slope (left) shows that compared to today, the less mountainous palaeogeography has more land area with very low surface gradients (<0.001; vertical black line), supporting the assumption in our carbon calculations (Methods) that the ancient topography was capable of supporting the same fractional area of wetland and peat formation (15-20%) as the modern topography. A similar analysis limited to permafrost zones is also shown (middle).
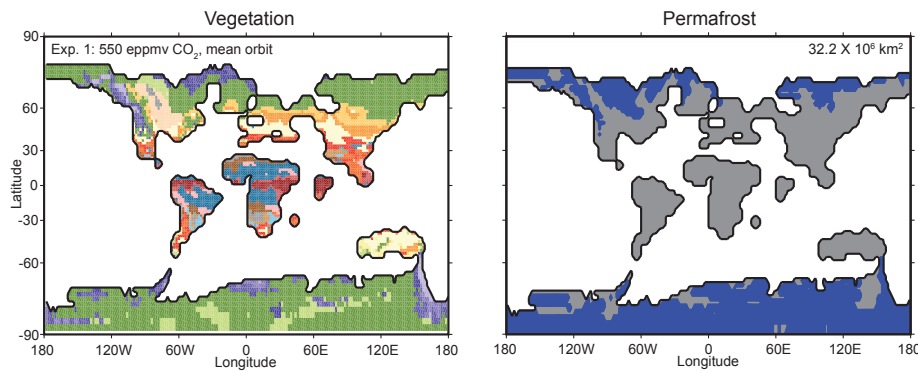
The paleogeographic reconstruction used here is conservative. Other, alternative reconstructions of East Antarctica[37,23,56,57] show a broad area of low relief in the continental interior (right) with >30% of the land area having surface slopes below 0.001 (dashed green line, middle panel)[37], about twice the fractional area of peatland assumed in our carbon calculations.
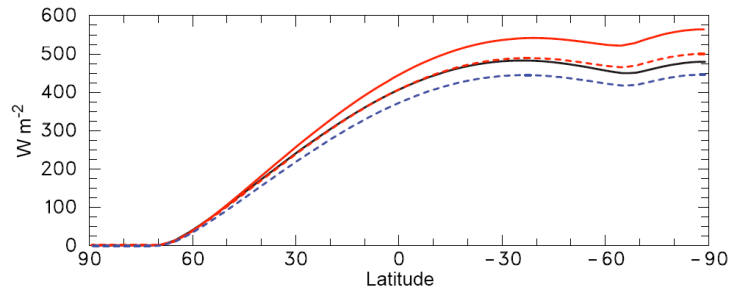
7. Modern Control Simulation

Supplementary Figure 7 | Modern control simulation of biomes and permafrost (Table 1). Vegetation types (left) correspond to those listed in Fig. 2. The area of the total permafrost region (right; $23.72 \times 10^6 \text{ km}^2$) compares favorably with observations $(22.79 \times 10^6 \text{ km}^2)$[35].

8. Experiment 1, 550 eppmv CO$_2$

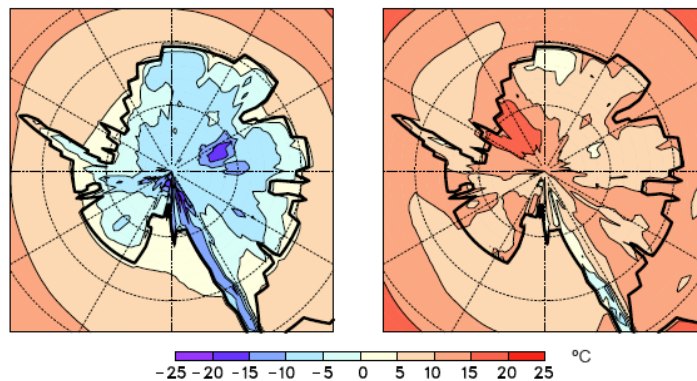**Supplementary Figure 8 | Exp. 1 biomes and vegetation.** Vegetation types (left) correspond to those listed in Fig. 2. The total permafrost area is 33% greater than in the modern control simulation, due to the available land area on Antarctica. However, the Antarctic temperatures are close to those allowing glaciation[58] and are therefore too cold to represent Pre-PETM conditions. Exp. 2 provides a better pre-PETM climatology.
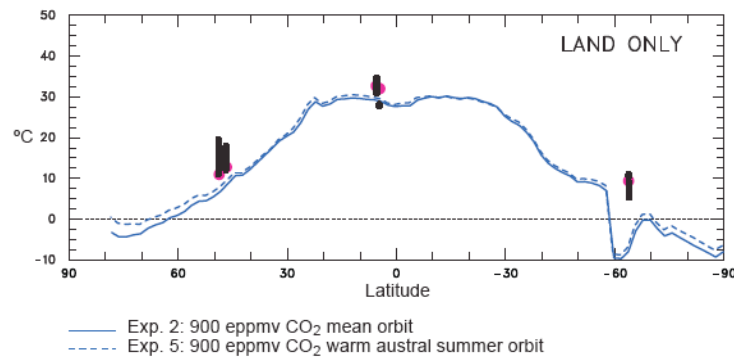
9. Orbital forcing

Supplementary Figure 9 | Austral summer (January) insolation. Monthly mean January insolation (top of the model atmosphere) with the range of orbits listed in Table 1. The solid black line is the mean orbital configuration with average obliquity, the dashed red line is the high-obliquity orbit, the solid red line is the high-obliquity and high-eccentricity orbit with perihelion in January, and the dashed blue line is the high-obliquity and high-eccentricity orbit with perihelion in July.

Supplementary Figure 10 | Antarctic surface air temperatures. Mean annual (left) and austral summer (DJF; right) surface (2m) air temperatures over Antarctica in the 900 eppmv CO_2 experiment with a mean orbit (Table 1, Exp 2). At these GHG levels, high latitude surface energy budgets and permafrost are especially sensitive to the applied orbital forcing shown in Figure S9.
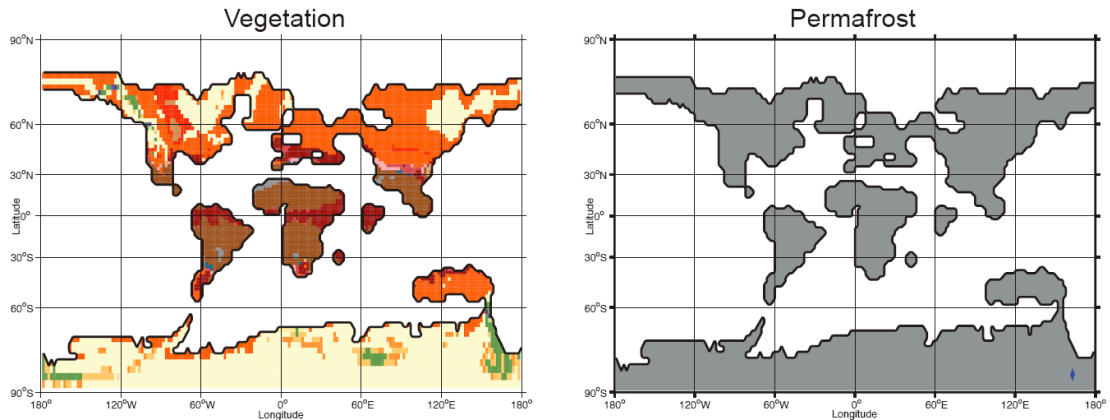
10. Mean Annual Temperatures at 900 eppmv CO$_2$

Exp. 2: 900 eppmv CO$_2$ mean orbit
Exp. 5: 900 eppmv CO$_2$ warm austral summer orbit

Supplementary Figure 11 | Simulated Terrestrial Mean Annual Temperatures in Exp. 2 compared with estimates of Late Paleocene MAT. Zonal means are shown for all land grid cells (solid and dashed blue lines) in two simulations with a mean orbit (solid blue line) and a high-eccentricity and high-obliquity orbit with perihelion in January (dashed blue line). In this GCM (with a "Charney" sensitivity to a doubling of CO$_2$ of 2.9 ºC), the orbitally driven reduction in permafrost area (7.37×10^6 km) is greatest at 900 eppmv CO$_2$. In cooler background climates with GHG levels below 900 eppmv CO$_2$, MATs remain cool enough to maintain significant permafrost in higher elevations, despite the orbital forcing. In warmer climates with GHGs above 900 eppmv CO$_2$, there is less initial permafrost to be affected by the orbital forcing, so the total permafrost area that undergoes thaw is smaller. Hence, the background climate state simulated at 900 eppmv CO$_2$ exhibits the greatest vulnerability to orbital forcing in terms of the potential for massive carbon release from the PFSC reservoir. In a warmer (post-PETM) climate, this potential is diminished because the PFSC reservoir is smaller, resulting in progressively smaller amplitude events through the steady warming of the Early Eocene (Fig. S1).
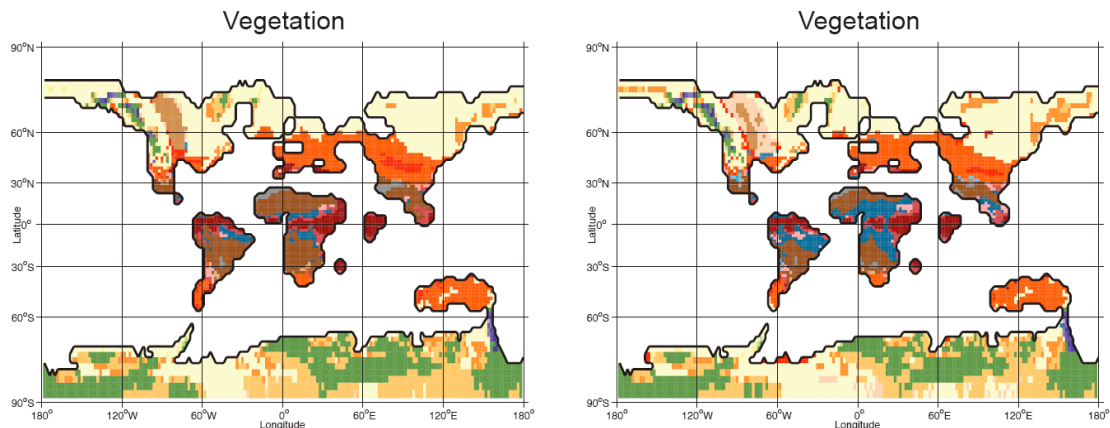
Black vertical bars show published estimates (including uncertainties) of late Paleocene MAT based on foliar analysis and faunal paleontological constraints[59-64]. Zonally averaged MATs from the GCM (blue lines) appear cooler than the data, because they include temperatures from high-elevation grid cells. Cold zonal average temperatures at 60ºS are an artifact of the narrow, high-elevation land bridge connecting Australia and Antarctica (Supplementary Fig. 2)[37,56]. High elevations are typically areas of erosion rather than fossil-preserving areas of deposition where most terrestrial proxy data are found, however lapse rate corrections between data and model temperatures are not applied in this case, because the ancient elevations of all proxy data locations are not known. A more direct comparison of regional model MATs (red dots) with the terrestrial proxy data (black bars) shows good model-data agreement even in the higher latitudes pertinent to permafrost. This indicates substantial permafrost in the higher elevations was indeed possible during these warm paleoclimates, and the simulated permafrost area in Exp. 2 (Fig 2a; Table 1) provides a reasonable representation of Late Paleocene (pre-PETM) conditions.

11. High GHG simulation at 5360 eppmv CO$_2$

Supplementary Figure 12 | Vegetation and permafrost with 5360 eppmv CO$_2$ (Exp. 8 in Table 1). Vegetation types (left) correspond to those listed in Fig 2. No tundra or permafrost exists at these elevated levels of GHGs.

12. Model sensitivity to high CO$_2$ concentrations in BIOME4

Supplementary Figure 13 | Response of simulated vegetation to high GHG concentrations in the GCM and fixed (low) CO$_2$ in BIOME4. The dependence of calculated vegetation distributions and NPP on prescribed CO$_2$ concentrations in BIOME4[33] was tested by re-running Exp. 6 (left panel; Table 1), with the same elevated GHG level (2680 eppmv CO$_2$) in the GCM, but with lower CO$_2$ (500 ppmv) in BIOME4 (right panel). Vegetation distributions are qualitatively similar and permafrost distributions are essentially unchanged, increasing confidence in the application of Biome4 to these high GHG scenarios.

13. Permafrost Soil Carbon reservoir calculations.

Table S1| Parameter values used to define PFSC ensemble members.

Peatland			Near Surface		Deep			
Ensemble Number	R (-)	ρ (kg m^{-3})	D (m)	R (-)	ρ (kg m^{-3})	D (m)	R (-)	ρ (kg m^{-3})	D (m)
1	0.1893	70	1.8	0.8107	21	2.5	0.057	30	22
2	0.1893	70	5.8	0.8107	21	2.5	0.057	30	22
3	0.1893	70	9.8	0.8107	21	2.5	0.057	30	22
4	0.1893	70	1.8	0.8107	30	2.5	0.057	30	22
5	0.1893	70	5.8	0.8107	30	2.5	0.057	30	22
6	0.1893	70	9.8	0.8107	30	2.5	0.057	30	22
7	0.1893	70	1.8	0.8107	21	D_{ave}	0.057	30	22
8	0.1893	70	5.8	0.8107	21	D_{ave}	0.057	30	22
9	0.1893	70	9.8	0.8107	21	D_{ave}	0.057	30	22
10	0.1893	70	1.8	0.8107	30	D_{ave}	0.057	30	22
11	0.1893	70	5.8	0.8107	30	D_{ave}	0.057	30	22
12	0.1893	70	9.8	0.8107	30	D_{ave}	0.057	30	22

Values of R, ρ_{perm}, and D used for peatland, near-surface, and deep PFSC deposits used in the 12-member ensemble (see Methods).
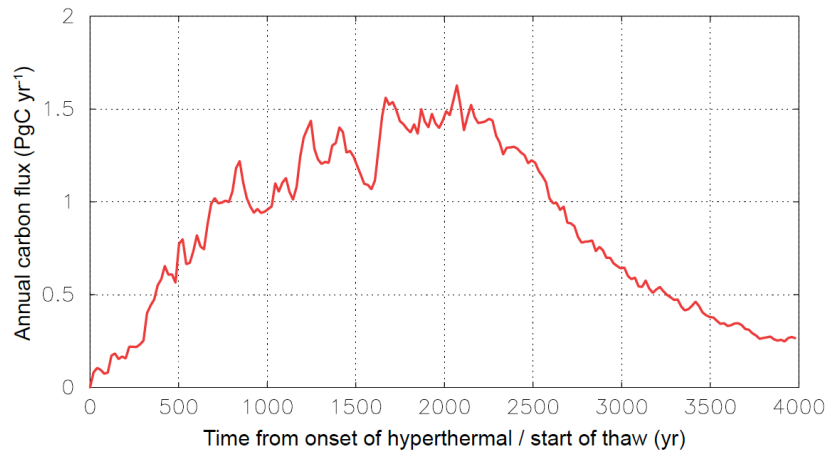
ADDITIONAL REFERENCES

47   Lunt, D. J., et al., A model for orbital pacing of methane hydrate destabilization during the Palaeogene, *Nature Geoscience* **4**, 775-778.

48   Christensen, T. R. et al., Factors controlling large scale variations in methane emissions from wetlands. *Geophysical Research Letters* **30** (7), 1414 (2003).

49   Allen, M. R. and Smith, L. A., Monte Carlo SSA: detecting irregular oscillations in the presence of coloured noise. *Journal of Climate* **9**, 3374 (1996).

50   Ghil, M. et al., Advanced spectral methods for climatic time series. *Reviews of Geophysics* **40** (1), 1003 (2002).

51   Westerhold, T. et al., On the duration of magnetochrons C24r and C25n and the timing of early Eocene global warming events: Implications from the Ocean Drilling Program Leg 208 Walvis Ridge depth transect. Paleoceanography **22**, PA2201 (2007).

52   Cramer, B. S., Wright, J. D., Kent, D. V., and Aubry, M.-P., Orbital climate forcing of $\delta^{13}C$ excursions in the late Paleocene–early Eocene (chrons C24n-C25n). *Paleoceanography* **18**, 1097 (2003).

53   Röhl, U. et al., The third and final Early Eocene thermal maximum: characteristics, timing and mechanisms of the 'X' event. *GSA Annual Meeting* **37**, 264 (2005).

54   Agnini, C. et al., An early Eocene carbon cycle perturbation at ~52.5 Ma in the Southern Alps: Chronology and biotic response. *Paleoceanography* **24** (2009).

55   Westerhold, T. and Rohl, U., High-resolution cyclostratigraphy of the early Eocene – new insights into the origin of the Cenozoic cooling trend. *Climates of the Past* **5** (3), 309-327 (2009).

56   Huber, M. and Sloan, L. C., Heat transport, deep waters, and thermal gradients: Coupled simulation of an Eocene Greenhouse Climate. *Geophysical Research Letters* **28** (18), 3481-3484 (2001).

57   Marwick, P. J. & Valdes, P. J. Palaeo-digital elevation models for use as boundary conditions in coupled ocean atmosphere GCM experiments: a Maastrichtian (late Cretaceous) example. *Palaeogeography, Palaeoclimatology, Palaeoecology* **213**, 37-63 (2004).

58   DeConto, R. M. et al., Thresholds for Cenozoic bipolar glaciation. *Nature* **455**, 653-656 (2008).

59   Currano, E. D., Labandeira, C. C., and Wilf, P., Fossil insect folivory tracks paleotemperature for six million years. *Ecological Monographs* **80** (4), 547-567 (2010).

60   Head, J. J. et al., Giant boid snake from the Palaeocene neotropics reveals hotter past equatorial temperatures. *Nature* **457**, 715-718 (2009).

61   Secord, R., Gingerich, P. D., Lohmann, K. C., and MacLeod, K. G., Continental warming preceding the Palaeocene–Eocene thermal maximum. *Nature* **467**, 955-958 (2010).

62   Wang, Q. et al., Climatic change during the Palaeocene to Eocene based on fossil plants from Fushun, China. *Palaeogeography, Palaeoclimatology, Palaeoecology* **295**, 323-331 (2010).

63   Wing, S. L. et al., Late Paleocene fossils from the Cerrejó Formation, Colombia, are the earliest record of Neotropical rainforest. *PNAS* **106** (44), 18627–18632 (2009).

64   Greenwood, D. R. and Wing, S. L., Eocene continental climates and latitudinal temperature gradients. *Geology* **23**, 1044-1048 (1995).

drives polar temperatures beyond the permafrost stability threshold in higher elevations (red dashed line). Time is shown from oldest (left) to youngest (right). The first (largest) event represents ETM1 (PETM), although the sequence of hyperthermals is purely illustrative. For clarity, the duration and timing of the events are not to scale and the orbital time series of polar climatic forcing (blue) is synthetic, drawn to broadly mimic the timing of the hyperthermal events relative to the composite polar orbital forcing shown in Figure 1. This sequence is similar to the recently proposed pacing of marine hydrate release events[47], although the terrestrial mechanism proposed here is different. The numbers (1-5) correspond to the schematic cross-sections of Antarctica shown below.

Five schematic cross sections (bottom panels) represent the conditions on Antarctica through a typical hyperthermal sequence. Corresponding cross sections of the northern high latitudes (with polar ocean bounded by continents) are not shown, but the same coeval sequence applies. At time 1 (corresponding to conditions in Fig. 2a), the permafrost stability threshold (red dashed line) is first exceeded. As noted in the text, extreme high-eccentricity and high-obliquity orbits thaw permafrost in both hemispheres simultaneously, regardless of the seasonal timing of perihelion (precession). The available PFSC reservoir at time 1 is the largest, having accumulated for $>10^6$ years during the cooler climates of the late Palaeocene. The initial PFSC release at time 2 (Fig. 2b) causes additional GHG warming, leading to the release of almost the entire PFSC reservoir within 10^4 years (Time 3; Fig. 2c). Once the PFSC reservoir is exhausted, polar latitudes are too warm for permafrost to reform or for PFSC stocks to recharge until some initial cooling occurs. Initial drawdown of CO_2 must be driven by other mechanisms, such as silicate weathering (black dashed line), enhanced in response to extreme global warmth and elevated precipitation rates. Once enough initial cooling allows permafrost to begin reforming in higher elevations (below the horizontal green line), PFSC stocks begin to recharge quickly in a positive feedback of CO_2 drawdown, cooling and expanding PFSC storage in lower elevations, all during a period of attenuated orbital forcing. This sequence may explain carbon isotopic records of ETM1 (PETM)[9], indicating a ~100-kyr delay in the recovery of the carbon cycle after the main carbon input, followed by rapid-paced recovery over the next ~50 kyr[9]. At time 5, the PFSC reservoir reaches its maximum potential, but remains smaller than at time 1, because the background climate state is warmer. The gradual warming trend is ongoing until the Early Eocene Climatic Optimum (Fig. 1), implying successively smaller PFSC reservoirs (and smaller release events) until the polar regions become too warm (beginning in the north polar regions) to support permafrost, even in high elevations.

2. Rate of carbon release from thawing permafrost

Supplementary Figure 2 | Estimated annual fluxes of carbon from thawing permafrost for the first hyperthermal event (PETM/ETM1). Carbon release at the onset of the PETM is calculated over a time period of 4000 years, assuming the time history of annual fluxes would be similar to a transient simulation of large-scale permafrost thaw and potential permafrost carbon release based on the Intergovernmental Panel on Climate Change (IPCC) A1B scenario[27]. Annual fluxes are scaled to match the release of 3434 PgC in the orbitally triggered warming sequence depicted in Fig 2. The annual fluxes increase to a peak at ~2100 years, representing the maximum thaw rate, and subsequently decline as the rate of thaw decreases.
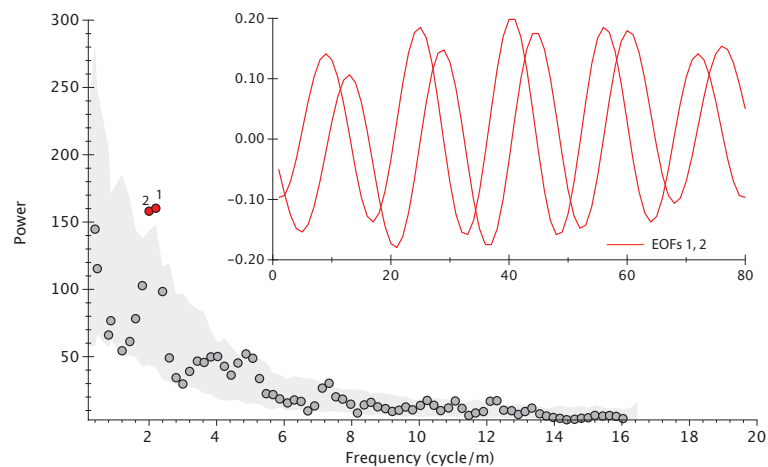
3. Composite Mean Summer Insolation Model

Assuming CO_2 release in high-latitude continental areas control the observed variability at Contessa Road and other sedimentary records, we estimate the effect of orbital forcing with a simple composite mean summer insolation model. The model assumes a linear relationship between changes in insolation and temperature, which is a conservative approach considering the enhanced climate sensitivity of high latitudes and the exponential relationship between soil temperature and background soil CH_4 emissions[48].

Because of different latitudinal distributions of polar continental areas between hemispheres, we use mean-summer insolation records at 75°S and 65°N from La04[18] for the time interval between 51.8-56.5 Ma, which includes ETM1, ETM2 and ETM3 and other minor hyperthermal-like events. To account for the larger extent of northern hemispheric land areas within orbitally sensitive high latitudes, we multiply the 65°N insolation curve by a factor of 2. Since Earth's orbital precession is antiphased between hemispheres, the resulting curve is dominated by obliquity (Fig 1e). A precessional signal is preserved because of the larger effect of the northern hemispheric curve, which accounts for geographic filtering. While variance at the 23-kyr precession period is observed in lower Eocene records[7,17,19], the orbital signal shows a weaker precessional component and becomes dominated by the 41 kyr obliquity period in time intervals corresponding with hyperthermals. These observations are well-matched by our GCM simulations (Fig. 1; Table 1), showing total global permafrost area is sensitive to obliquity forcing, once a threshold of background warming is reached. In the model, total permafrost area is most sensitive to a combination of high obliquity and high eccentricity (increased seasonality), with perihelion occurring in either January or July. The sensitivity of modeled permafrost to either intense summer insolation or longer summers (increased total integrated insolation) also has the effect of attenuating the precession signal, because total permafrost is reduced in both hemispheres simultaneously, regardless of the phase of precession. In this case, the smallest permafrost inventories at a given set of GHG levels occur during a combination of high obliquity and high eccentricity orbits, corresponding with the onset of hyperthermals shown in Figure 1.
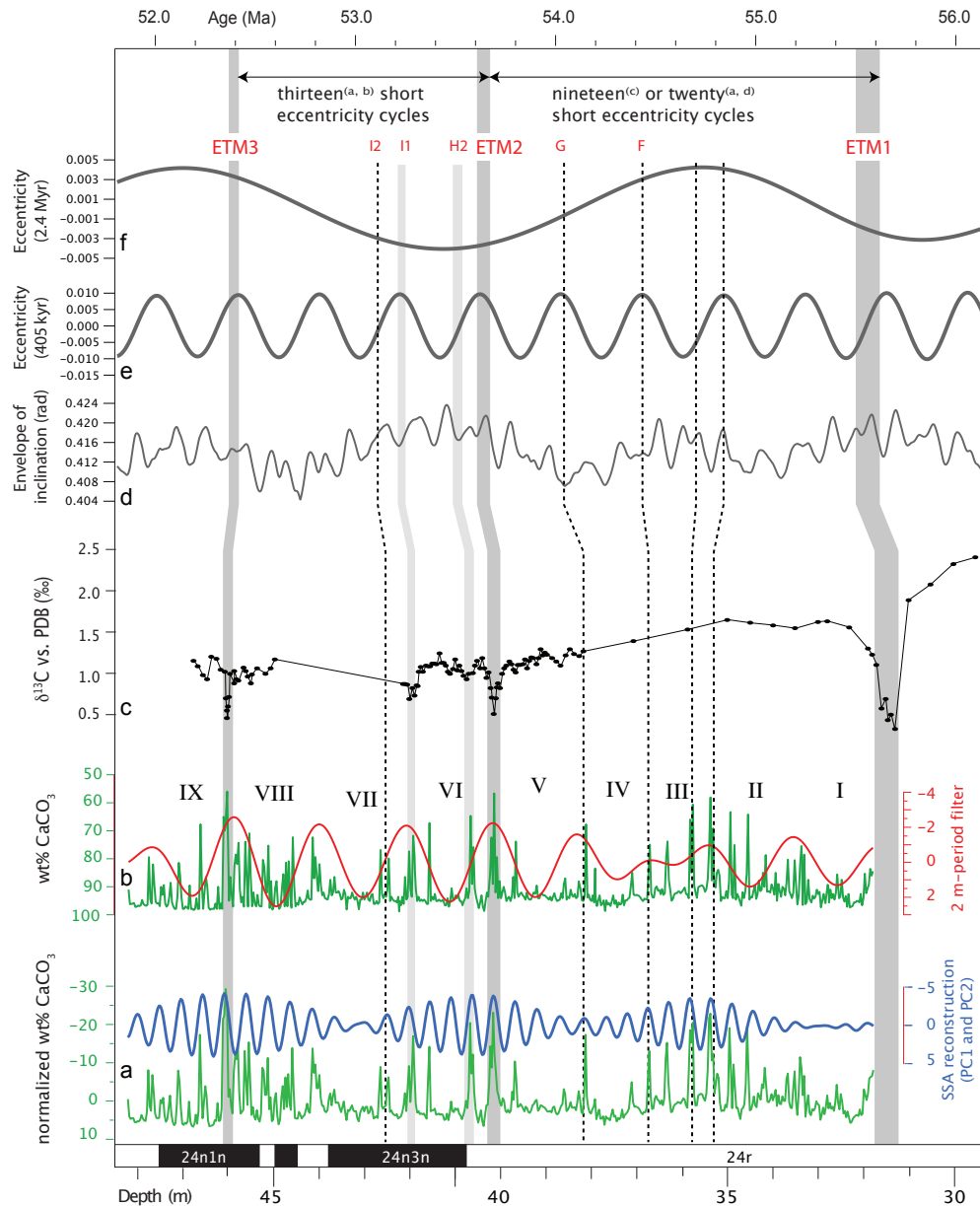
4. Singular Spectrum Analysis of the Wt% CaCO₃ Record

Singular spectrum analysis (SSA) is used to recognize harmonic components in the Wt% CaCO$_3$ record in the depth domain, which we validate using a Monte Carlo method[49] with a confidence limit of 97.5%. SSA is particularly well suited for the analysis of complex system showing non-linear oscillations on multiple time scales, like the climate system[50]. SSA is used here with an embedding dimension of 80. A longer embedding dimension would offer the advantage of detecting longer-term components and higher spectral resolution. However, an embedding dimension of 80 is a good choice for our series (550 points with 3 cm sampling rate) and an expected oscillatory period of ~50 cm for short eccentricity[7]. This approach provides a statistically robust means of detecting harmonic components in the range of orbital frequencies and their modulation before tuning (i.e. in the depth domain). Furthermore, cycle counting of the statistically significant components that are recognized to reflect orbital forcing offers an additional tool for comparison with previously published floating chronologies for the interval under investigation[17,19,51]. In the SSA, harmonic components typically occur as distinct oscillatory pairs of eigenvectors characterized by the same dominant frequency, similar eigenvalues, and a Pi/2 phase lag of their Empirical Orthogonal Functions (EOFs). Harmonic components have been identified in EOFs 1 and 2, both of which are above the 97.5% confidence level (Fig. S1), based on a Monte Carlo test against red-noise[49]. The sum of the two largest EOFs (EOF1 and EOF2) accounts for ~14% of the signal variance and the reconstructed component (Fig. S2) and shows a close correspondence to the original Wt% CaCO$_3$ signal. The SSA-reconstructed component also shows a distinct peak of spectral power with a period of ca. 0.48 metres, which is the period expected for the short eccentricity cycle based on a 4.7 m/Myr average sedimentation rate of the lower Eocene Contessa Road section as derived from independent (magneto- and bio-stratigraphic) dating[7]. The amplitude of short eccentricty cycles in the CaCO$_3$ record is modulated by a long-term forcing showing three maxima, all corresponding to hyperthermal events in the depth domain. Once the section is tuned in the time domain (based on cycle counting and an absolute age of 55.7 Ma for the base of ETM1)[7,19], these three modulation maxima (major hyperthermal events) coincide with the (sole) three maxima occurring in the composite mean summer insolation curve within the studied interval (see panel E in Figure 1 of the main text). A fourth maximum in the composite mean summer insolation is centered out of the surveyed interval at ~ 55.7 Ma at the onset of PETM, reinforcing the evidence for a 100% match between intervals of warmer summers at high latitudes and ETMs. Some uncertainty remains in terms of the absolute age of the ETMs and the astronomical solution (providing an absolute age of maxima in the composite mean summer insolation), however, the combined effect of the long-term components of eccentricity (400 kyr) and obliquity (1.2 Myr) produces a succession of high latitude insolation maxima that is 100% matched by the long-term cyclical architecture of lower Eocene sedimentary and geochemical records.
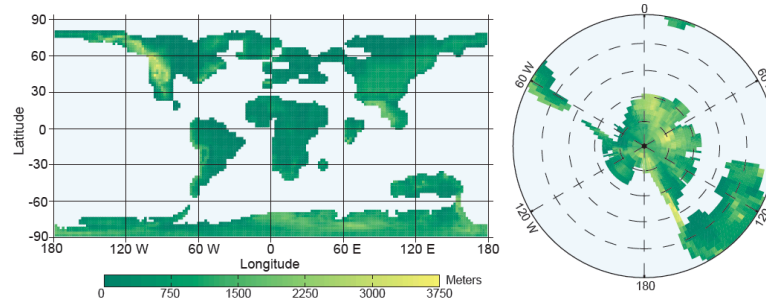
Supplementary Figure 3 | SSA Analysis. SSA Eigenspectrum and statistically significant (>97.5%) EOFs (inset) according to a red noise Monte Carlo Test of the $CaCO_3$ record.
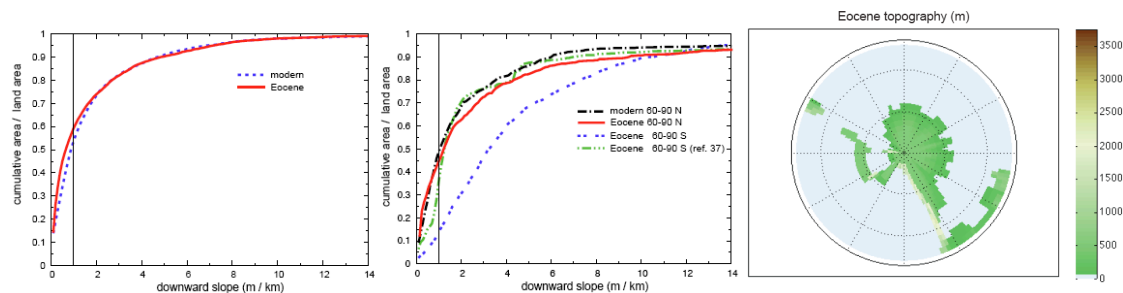
5. Orbital phasing of Early Eocene Hyperthermals

Supplementary Figure 4 | Orbital Phasing. The lower Eocene $CaCO_3$, $\delta^{13}C$ and magnetostratigraphic records from the Contessa Road section (lower panels). Extraction of the long eccentricity component (405 kyr; red line) from the CaCO3 record (green line) allows a fine-scale calibration to the long-term (405 kyr and 2.4 Myr) eccentricity components and the Hilbert transform of the obliquity from the La04[18] astronomical solution (top three panels). SSA reconstruction of the harmonic components (110 kyr; blue line) allows counting of individual eccentricity cycles. Maximum modulation occurs across intervals of concomitant high eccentricity and high obliquity, corresponding to the inferred position of CIE events in published cyclochronologies of the same interval[19,51-55]. The number of short eccentricity cycles counted in different sedimentary settings by a[55], b[7]; c[17], and d[51] are shown at top.
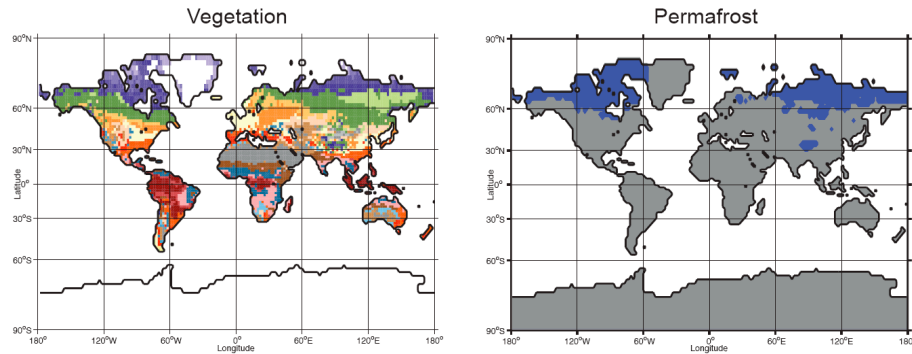
6. Model Boundary Conditions

Supplementary Figure 5 | Early Eocene global paleogeography. Palaeocene-Eocene climate-vegetation-permafrost simulations use a prior paleogeographic reconstruction of the Eocene[37,56], with Antarctic shorelines and elevations replaced with a new, larger reconstruction of West Antarctica in latest Eocene time[21]. The global 2º×2º cylindrical equidistant reconstruction used by the GCM surface model grid is shown at left, with a south polar view shown at right. In East Antarctica, where detailed geological data are lacking, the topography[21] is based on modern sub-glacial elevations, isostatically compensated to reflect ice-free conditions.

Supplementary Figure 6 | Palaeocene-Eocene hypsometry. The cumulative (fractional) land area below a given surface slope (left) shows that compared to today, the less mountainous palaeogeography has more land area with very low surface gradients (<0.001; vertical black line), supporting the assumption in our carbon calculations (Methods) that the ancient topography was capable of supporting the same fractional area of wetland and peat formation (15-20%) as the modern topography. A similar analysis limited to permafrost zones is also shown (middle).
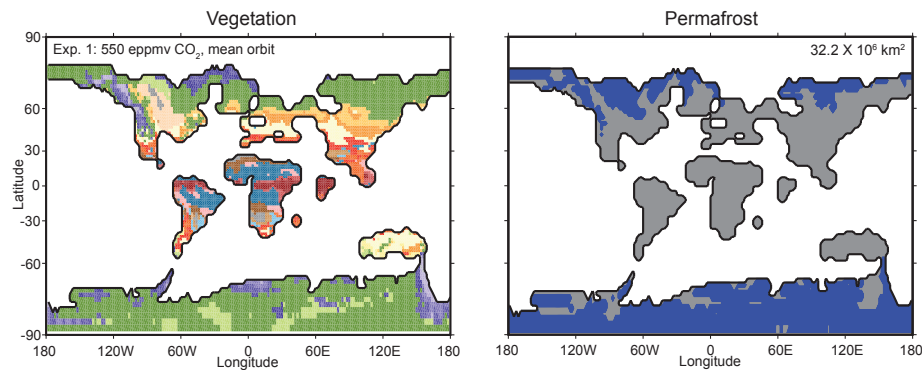
The paleogeographic reconstruction used here is conservative. Other, alternative reconstructions of East Antarctica[37,23,56,57] show a broad area of low relief in the continental interior (right) with >30% of the land area having surface slopes below 0.001 (dashed green line, middle panel)[37], about twice the fractional area of peatland assumed in our carbon calculations.
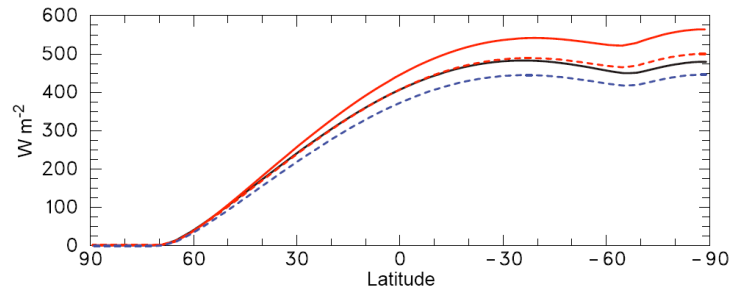
7. Modern Control Simulation

Supplementary Figure 7 | Modern control simulation of biomes and permafrost (Table 1). Vegetation types (left) correspond to those listed in Fig. 2. The area of the total permafrost region (right; 23.72×10^6 km^2) compares favorably with observations $(22.79 \times 10^6$ km$^2)$[35].
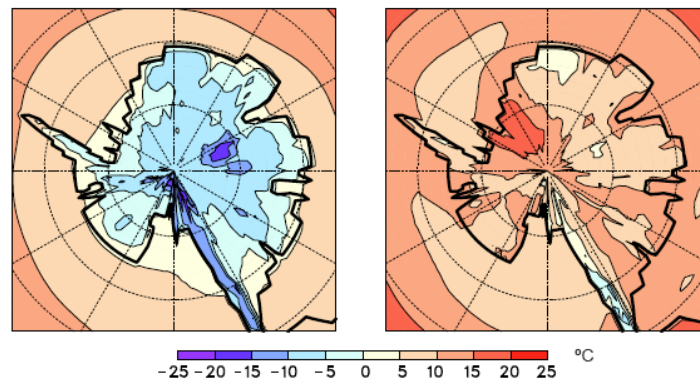
8. Experiment 1, 550 eppmv CO$_2$

Supplementary Figure 8 | Exp. 1 biomes and vegetation. Vegetation types (left) correspond to those listed in Fig. 2. The total permafrost area is 33% greater than in the modern control simulation, due to the available land area on Antarctica. However, the Antarctic temperatures are close to those allowing glaciation[58] and are therefore too cold to represent Pre-PETM conditions. Exp. 2 provides a better pre-PETM climatology.
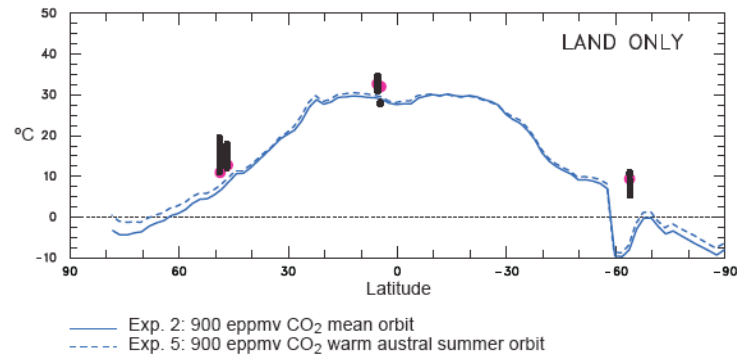
9. Orbital forcing

Supplementary Figure 9 | Austral summer (January) insolation. Monthly mean January insolation (top of the model atmosphere) with the range of orbits listed in Table 1. The solid black line is the mean orbital configuration with average obliquity, the dashed red line is the high-obliquity orbit, the solid red line is the high-obliquity and high-eccentricity orbit with perihelion in January, and the dashed blue line is the high-obliquity and high-eccentricity orbit with perihelion in July.

Supplementary Figure 10 | Antarctic surface air temperatures. Mean annual (left) and austral summer (DJF; right) surface (2m) air temperatures over Antarctica in the 900 eppmv CO_2 experiment with a mean orbit (Table 1, Exp 2). At these GHG levels, high latitude surface energy budgets and permafrost are especially sensitive to the applied orbital forcing shown in Figure S9.
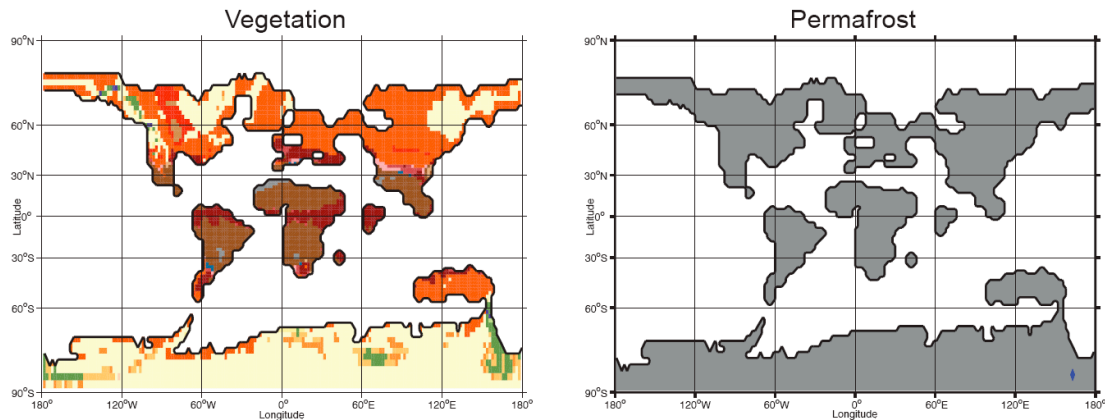
10. Mean Annual Temperatures at 900 eppmv CO₂

Supplementary Figure 11 | Simulated Terrestrial Mean Annual Temperatures in Exp. 2 compared with estimates of Late Paleocene MAT. Zonal means are shown for all land grid cells (solid and dashed blue lines) in two simulations with a mean orbit (solid blue line) and a high-eccentricity and high-obliquity orbit with perihelion in January (dashed blue line). In this GCM (with a "Charney" sensitivity to a doubling of CO_2 of 2.9 ºC), the orbitally driven reduction in permafrost area (7.37×10^6 km) is greatest at 900 eppmv CO_2. In cooler background climates with GHG levels below 900 eppmv CO_2, MATs remain cool enough to maintain significant permafrost in higher elevations, despite the orbital forcing. In warmer climates with GHGs above 900 eppmv CO_2, there is less initial permafrost to be affected by the orbital forcing, so the total permafrost area that undergoes thaw is smaller. Hence, the background climate state simulated at 900 eppmv CO_2 exhibits the greatest vulnerability to orbital forcing in terms of the potential for massive carbon release from the PFSC reservoir. In a warmer (post-PETM) climate, this potential is diminished because the PFSC reservoir is smaller, resulting in progressively smaller amplitude events through the steady warming of the Early Eocene (Fig. S1).
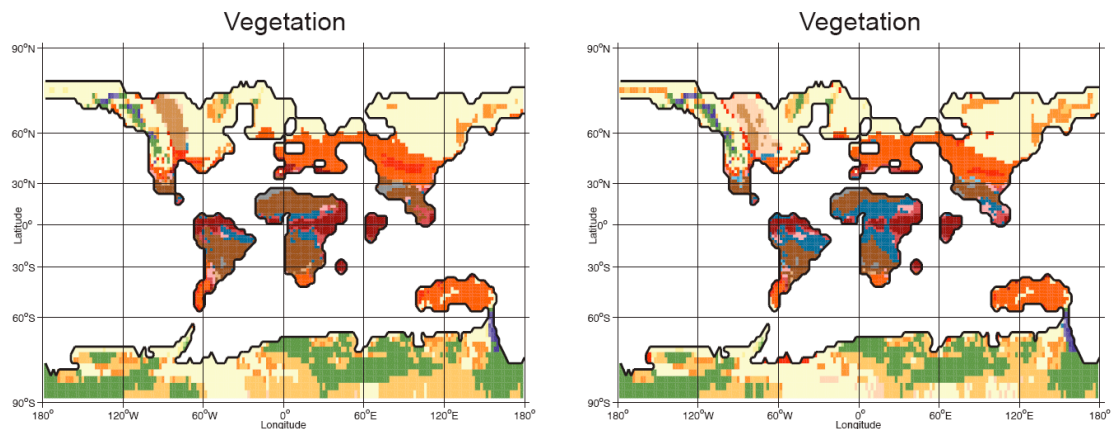
Black vertical bars show published estimates (including uncertainties) of late Paleocene MAT based on foliar analysis and faunal paleontological constraints[59-64]. Zonally averaged MATs from the GCM (blue lines) appear cooler than the data, because they include temperatures from high-elevation grid cells. Cold zonal average temperatures at 60ºS are an artifact of the narrow, high-elevation land bridge connecting Australia and Antarctica (Supplementary Fig. 2)[37,56]. High elevations are typically areas of erosion rather than fossil-preserving areas of deposition where most terrestrial proxy data are found, however lapse rate corrections between data and model temperatures are not applied in this case, because the ancient elevations of all proxy data locations are not known. A more direct comparison of regional model MATs (red dots) with the terrestrial proxy data (black bars) shows good model-data agreement even in the higher latitudes pertinent to permafrost. This indicates substantial permafrost in the higher elevations was indeed possible during these warm paleoclimates, and the simulated permafrost area in Exp. 2 (Fig 2a; Table 1) provides a reasonable representation of Late Paleocene (pre-PETM) conditions.

11. High GHG simulation at 5360 eppmv CO$_2$

Supplementary Figure 12 | Vegetation and permafrost with 5360 eppmv CO$_2$ (Exp. 8 in Table 1). Vegetation types (left) correspond to those listed in Fig 2. No tundra or permafrost exists at these elevated levels of GHGs.

12. Model sensitivity to high CO$_2$ concentrations in BIOME4

Supplementary Figure 13 | Response of simulated vegetation to high GHG concentrations in the GCM and fixed (low) CO$_2$ in BIOME4. The dependence of calculated vegetation distributions and NPP on prescribed CO$_2$ concentrations in BIOME4[33] was tested by re-running Exp. 6 (left panel; Table 1), with the same elevated GHG level (2680 eppmv CO$_2$) in the GCM, but with lower CO$_2$ (500 ppmv) in BIOME4 (right panel). Vegetation distributions are qualitatively similar and permafrost distributions are essentially unchanged, increasing confidence in the application of Biome4 to these high GHG scenarios.

13. Permafrost Soil Carbon reservoir calculations.

Table S1| Parameter values used to define PFSC ensemble members.

Peatland			Near Surface			Deep			
Ensemble Number	R (-)	ρ (kg m^{-3})	D (m)	R (-)	ρ (kg m^{-3})	D (m)	R (-)	ρ (kg m^{-3})	D (m)
1	0.1893	70	1.8	0.8107	21	2.5	0.057	30	22
2	0.1893	70	5.8	0.8107	21	2.5	0.057	30	22
3	0.1893	70	9.8	0.8107	21	2.5	0.057	30	22
4	0.1893	70	1.8	0.8107	30	2.5	0.057	30	22
5	0.1893	70	5.8	0.8107	30	2.5	0.057	30	22
6	0.1893	70	9.8	0.8107	30	2.5	0.057	30	22
7	0.1893	70	1.8	0.8107	21	D_{ave}	0.057	30	22
8	0.1893	70	5.8	0.8107	21	D_{ave}	0.057	30	22
9	0.1893	70	9.8	0.8107	21	D_{ave}	0.057	30	22
10	0.1893	70	1.8	0.8107	30	D_{ave}	0.057	30	22
11	0.1893	70	5.8	0.8107	30	D_{ave}	0.057	30	22
12	0.1893	70	9.8	0.8107	30	D_{ave}	0.057	30	22

Values of R, ρ_{perm}, and D used for peatland, near-surface, and deep PFSC deposits used in the 12-member ensemble (see Methods).

ADDITIONAL REFERENCES

47 Lunt, D. J., et al., A model for orbital pacing of methane hydrate destabilization during the Palaeogene, *Nature Geoscience* **4**, 775-778.

48 Christensen, T. R. et al., Factors controlling large scale variations in methane emissions from wetlands. *Geophysical Research Letters* **30** (7), 1414 (2003).

49 Allen, M. R. and Smith, L. A., Monte Carlo SSA: detecting irregular oscillations in the presence of coloured noise. *Journal of Climate* **9**, 3374 (1996).

50 Ghil, M. et al., Advanced spectral methods for climatic time series. *Reviews of Geophysics* **40** (1), 1003 (2002).

51 Westerhold, T. et al., On the duration of magnetochrons C24r and C25n and the timing of early Eocene global warming events: Implications from the Ocean Drilling Program Leg 208 Walvis Ridge depth transect. Paleoceanography **22**, PA2201 (2007).

52 Cramer, B. S., Wright, J. D., Kent, D. V., and Aubry, M.-P., Orbital climate forcing of δ^{13}C excursions in the late Paleocene–early Eocene (chrons C24n-C25n). *Paleoceanography* **18**, 1097 (2003).

53 Röhl, U. et al., The third and final Early Eocene thermal maximum: characteristics, timing and mechanisms of the 'X' event. *GSA Annual Meeting* **37**, 264 (2005).

54 Agnini, C. et al., An early Eocene carbon cycle perturbation at ∼52.5 Ma in the Southern Alps: Chronology and biotic response. *Paleoceanography* **24** (2009).

55 Westerhold, T. and Rohl, U., High-resolution cyclostratigraphy of the early Eocene – new insights into the origin of the Cenozoic cooling trend. *Climates of the Past* **5** (3), 309-327 (2009).

56 Huber, M. and Sloan, L. C., Heat transport, deep waters, and thermal gradients: Coupled simulation of an Eocene Greenhouse Climate. *Geophysical Research Letters* **28** (18), 3481-3484 (2001).

57 Marwick, P. J. & Valdes, P. J. Palaeo-digital elevation models for use as boundary conditions in coupled ocean atmosphere GCM experiments: a Maastrichtian (late Cretaceous) example. *Palaeogeography, Palaeoclimatology, Palaeoecology* **213**, 37-63 (2004).

58 DeConto, R. M. et al., Thresholds for Cenozoic bipolar glaciation. *Nature* **455**, 653-656 (2008).

59 Currano, E. D., Labandeira, C. C., and Wilf, P., Fossil insect folivory tracks paleotemperature for six million years. *Ecological Monographs* **80** (4), 547-567 (2010).

60 Head, J. J. et al., Giant boid snake from the Palaeocene neotropics reveals hotter past equatorial temperatures. *Nature* **457**, 715-718 (2009).

61 Secord, R., Gingerich, P. D., Lohmann, K. C., and MacLeod, K. G., Continental warming preceding the Palaeocene–Eocene thermal maximum. *Nature* **467**, 955-958 (2010).

62 Wang, Q. et al., Climatic change during the Palaeocene to Eocene based on fossil plants from Fushun, China. *Palaeogeography, Palaeoclimatology, Palaeoecology* **295**, 323-331 (2010).

63 Wing, S. L. et al., Late Paleocene fossils from the Cerrejó Formation, Colombia, are the earliest record of Neotropical rainforest. *PNAS* **106** (44), 18627–18632 (2009).

64   Greenwood, D. R. and Wing, S. L., Eocene continental climates and latitudinal temperature gradients. *Geology* **23**, 1044-1048 (1995).